Author's personal copy

Available online at www.sciencedirect.com

SciVerse ScienceDirect

Acta Materialia 60 (2012) 1099–1115

Acta MATERIALIA

www.elsevier.com/locate/actamat

Non-crystallographic shear banding in crystal plasticity FEM simulations: Example of texture evolution in α-brass

N. Jia [a,b], F. Roters [b], P. Eisenlohr [b], C. Kords [b], D. Raabe [b,*]

[a] Key Laboratory for Anisotropy and Texture of Materials (MOE), Northeastern University, Shenyang 110004, China
[b] Max-Planck-Institut für Eisenforschung, D-40237 Düsseldorf, Germany

Received 29 July 2011; received in revised form 8 September 2011; accepted 24 October 2011

Abstract

We present crystal plasticity finite element simulations of the texture evolution in α-brass polycrystals under plane strain compression. The novelty is a non-crystallographic shear band mechanism [Anand L, Su C. J Mech Phys Solids 2005;53:1362] that is incorporated into the constitutive model in addition to dislocation and twinning. Non-crystallographic deformation associated with shear banding leads to weaker copper and S texture components and to a stronger brass texture compared to simulations enabling slip and twinning only. The lattice rotation rates are reduced when shear banding occurs. This effect leads to a weaker copper component. Also, the initiation of shear banding promotes brass-type components. In summary the occurrence of non-crystallographic deformation through shear bands shifts face-centered-cubic deformation textures from the copper type to the brass type.
© 2011 Acta Materialia Inc. Published by Elsevier Ltd. All rights reserved.

Keywords: Texture; Shear bands; Finite element analysis

1. Introduction

Polycrystalline face-centered-cubic (fcc) metals usually deform via dislocations, twins, and shear bands. This leads to pronounced plastic anisotropy at the grain scale and to preferred grain orientation distributions, i.e. crystallographic textures. Rolling textures of fcc metals range between two types, i.e. the brass-type texture and the copper-type texture [1–4]. The stacking fault energy (SFE) plays an important role for the prevailing mechanisms of plastic deformation and the resultant textures [4,5]. For aluminum and other fcc materials with high SFE, dislocation glide is the main mechanism during cold rolling and the $\{112\}\langle111\rangle$ (copper) and $\{123\}\langle634\rangle$ (S) texture components (copper-type textures) are developed [1–5]. In contrast, in Cu–30 wt.% Zn (α-brass) and related metals and alloys with low SFE, mechanical twinning and shear banding occur together with dislocation glide as main deformation carriers, particularly at large plastic deformations. The resulting rolling textures are characterized by the $\{011\}\langle211\rangle$ (brass) and $\{011\}\langle100\rangle$ (Goss) components (brass-type texture). Investigations on deformation structures and textures of low SFE materials can be traced back to the early work by Wassermann [3] and during the past 60 years numerous further studies have appeared. In Cu–Zn alloys [1,2,5], austenitic stainless steels [6,7], silver [8,9], and Cu–Al alloys [9,10] fine twins were observed at low strains when subjected to plane strain compression or cold rolling. It is also suggested that dense twin boundaries inhibit homogeneous dislocation glide, which can lead to instabilities. Hence, at large deformations shear bands cover large volume fractions and play a major role in accommodating the imposed deformation in fcc metals and alloys with low SFE [1,2,6,8–10]. Local orientation measurements using transmission electron microscopy (TEM) suggest that shear bands that cut through profuse twins have a decisive effect on the texture change from the copper to the brass type [8,11]. Recent investigations reveal that shear bands in the form of narrow band-like

* Corresponding author.
E-mail address: d.raabe@mpie.de (D. Raabe).

1359-6454/$36.00 © 2011 Acta Materialia Inc. Published by Elsevier Ltd. All rights reserved.
doi:10.1016/j.actamat.2011.10.047

Author's personal copy

regions of concentrated non-crystallographic plastic flow with nano-sized internal structure expand into the abutting twin/matrix structure [12,13]. These studies suggest that shear banding induced texture evolution in fcc alloys might be profoundly different from crystal rotations that originate from dislocation and twinning shear alone.

In the past decades, attention was placed on the quantitative prediction of crystalline anisotropy and the resulting texture evolution of fcc metals [14–28]. Among the various simulation approaches, the crystal plasticity finite element (CPFE) models have gained momentum in capturing crystalline anisotropy, in-grain and inter-grain micromechanical response, and texture evolution [14–17,19–21,23–26,28,29]. Other successful approaches to texture evolution include advanced grain-interaction models [30–32] and self-consistent methods [33,34]. Recently, highly efficient Fast Fourier solvers have gained relevance in this field [35,36]. The different models have been applied successfully to the quantitative prediction of aluminum textures by correspondingly adjusting constitutive parameters [25,30,37]. In contrast, for alloys with low SFE, models that accurately predict textures and anisotropy remain a challenge. Specifically, the quantitative consideration of the effect of non-crystallographic deformation associated with shear bands that were experimentally observed to contribute to the texture transition from the copper to the brass type, was not yet achieved. So far only a few studies have addressed the simulation of deformation textures of low SFE fcc metals incorporating shear band theory. By superposing a shear strain on the material within shear bands, Gil Sevillano et al. [38] focused on the influence of macroscale shear bands on deformation textures. They reported that with this treatment shear bands did not show a significant effect on the development of the brass-type texture. On the other hand, Kalidindi [23] conducted simulations by introducing a specified shear component stemming from shear bands into the velocity gradient tensor for grains whose twin volume fraction reaches a critical value. He observed that the mechanism of shear banding contributed to the copper-to-brass texture transition. These studies suggest that if non-crystallographic deformation is introduced into micromechanical models, a quantitative prediction of brass-type textures could be achieved.

Therefore, in this work a shear band model is used to simulate texture evolution of α-brass under plane strain compression. Since shear bands induce non-crystallographic deformation we adopt the model of Anand et al. [39] that was originally designed for amorphous materials. Based on an existing CPFE constitutive model that incorporates dislocation and twinning shear [20,21,28,40], the new approach assumes additionally that shear banding occurs via six specific shear band systems. The potential systems, defined relative to the principal directions of the second Piola–Kirchoff stress (conjugated to the elastic Green–Lagrange strain), are activated when a critical stress for shear band formation is reached at a material point [39]. The plastic velocity gradient is then modified by the contribution due to shear banding in addition to that provided by crystallographic shear (from dislocations and twins). Our simulations show that with increasing deformation the occurrence of non-crystallographic shear banding weakens the copper and S texture components relative to the strengthened brass component. Besides this effect on texture evolution the simulation results also provide fundamental insight into the micromechanics of deformation texture evolution in low SFE fcc materials. Also it helps us to better understand the constitutive parameters that promote shear banding. These insights are important for the design and application of engineering materials that contain fcc metallic phases with low SFE [41].

2. Experiments

2.1. Material and experimental procedures

The studied material is α-brass (Cu–30 wt.% Zn), which is a low SFE fcc alloy. The material was cross-rolled to a total engineering thickness reduction of 30% and annealed at 260 °C for 1.5 h to provide an equiaxed microstructure with an average grain size of ~30 μm [2]. This was the starting material in the current study. Subsequently, the alloy was symmetrically rolled at room temperature to different thickness reductions of 20%, 40%, 80%, and 90%. Textures were measured in the center (mid-thickness) layer. The {111}, {200}, and {220} pole figures were obtained using X-ray diffraction (XRD) with Cu Kα radiation in reflection geometry. Crystallographic orientation distribution functions (ODFs) were determined from the pole figures by using the Labo-Tex texture analysis software [42]. The notation of $\{hkl\}\langle uvw\rangle$ was used for characterizing the texture type with $\{hkl\} \parallel \mathrm{ND}$ and $\langle uvw\rangle \parallel \mathrm{RD}$, where RD is the rolling direction, TD the transverse direction, and ND the normal direction of the sheet.

2.2. Rolling textures measured by XRD

The ODF sections ($\varphi_2 = 0°$, 45° and 65° in Euler space) of the initial specimen for α-brass are displayed in Fig. 1a, indicating that the initial texture in the annealed material is practically random. The same ODF sections of the cold-rolled materials at different reductions are also shown. The ideal orientations of the main texture components are presented in Fig. 1b. Below 40% reduction, several texture components, including brass, Goss, copper, S, and $\{124\}\langle 211\rangle$ (R) are formed. These components are typically found in rolled fcc metals [1–6]. At 80% reduction, the rolling textures consist of the pronounced brass and {111} fiber components as well as of the R and S components. The brass component dominates over the other orientations. After 90% reduction, a very sharp brass component appears, which is typical of fcc metals with low SFE at large strains [1–4]. Weak R and S components are also found. In addition to the Euler space sections, we

Author's personal copy

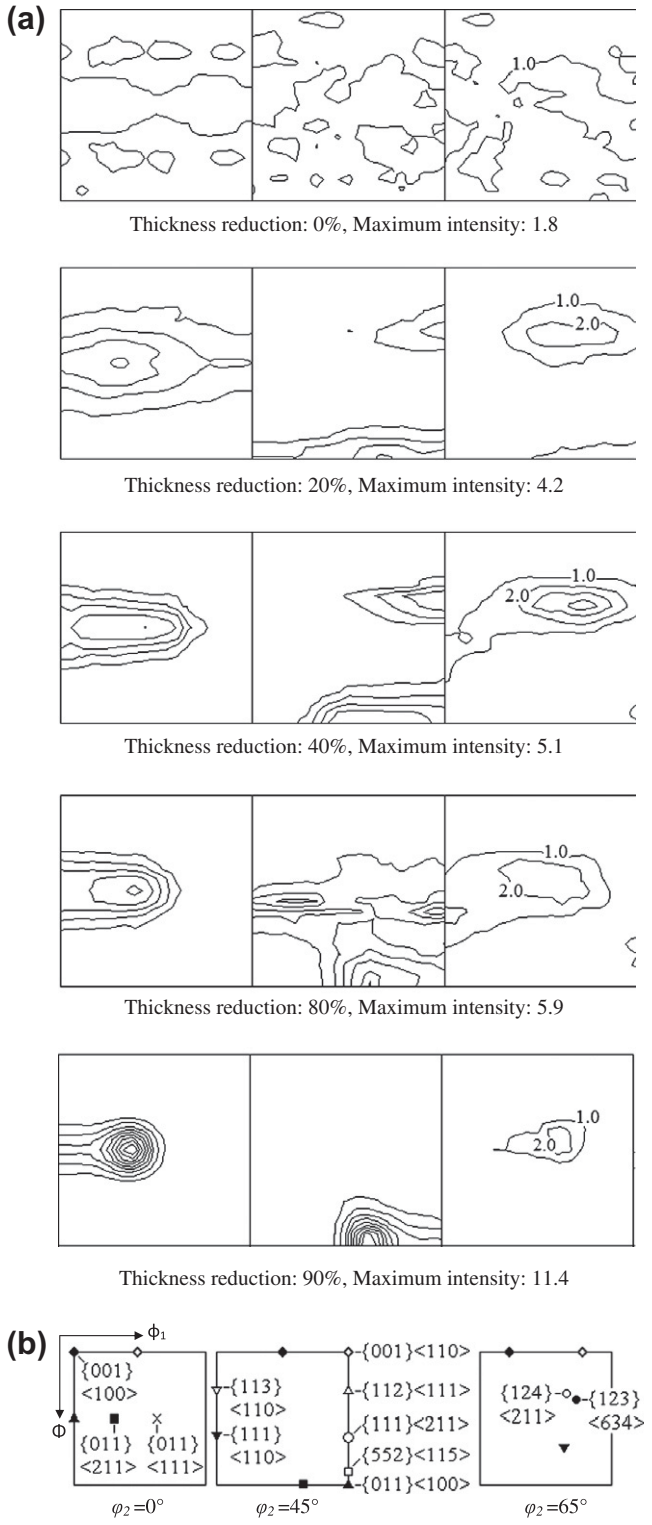

Fig. 1. (a) ODF sections determined via X-ray diffraction at constant angles φ_2 (0°, 45° and 65°) showing texture evolution of cold rolled α-brass at different thickness reductions (0%, 20%, 40%, 80%, and 90% as marked beneath the corresponding figures). (b) Schematic sketch showing the ideal positions of the main texture components.

also apply texture fiber diagrams [43] and sections in Rodrigues space [44] for the quantitative comparison of textures obtained from experiments and simulations.

3. Simulation procedures

3.1. Constitutive formulations

In this work, a CPFE model is developed to simulate the texture evolution in α-brass. The novelty of the approach consists in using a constitutive model that incorporates shear banding in conjunction with dislocation slip and mechanical twinning. For the latter two concepts we refer to the work of Roters, Eisenlohr and co-workers [28,40,45], and for non-crystallographic shear bands to the model of Anand et al. [39].

3.1.1. Kinematics

We use the finite strain kinematic framework in which the deformation gradient, $\mathbf{F}$, is multiplicatively decomposed into the plastic, $\mathbf{F}^{\mathrm{p}}$, and "elastic", $\mathbf{F}^{\mathrm{e}}$, deformation gradients according to:

$$\mathbf{F} = \mathbf{F}^{\mathrm{e}}\mathbf{F}^{\mathrm{p}} \tag{1}$$

The initial plastic deformation gradient $\mathbf{F}_0^{\mathrm{p}}$ is set to the inverse of the local crystal orientation, $\mathbf{T}_0^{-1}$, and evolves at a rate governed by the plastic velocity gradient $\mathbf{L}^{\mathrm{p}}$:

$$\dot{\mathbf{F}}^{\mathrm{p}} = \mathbf{L}^{\mathrm{p}}\mathbf{F}^{\mathrm{p}} \tag{2}$$

The evolution of the crystal orientation with strain then follows from the polar decomposition $\mathbf{F}^{\mathrm{e}} = \mathbf{R}^{\mathrm{e}}\mathbf{U}^{\mathrm{e}}$ as $\mathbf{T} = \mathbf{R}^{\mathrm{e}}$. It is assumed that any twinned part of the matrix maintains a perfect (twin) orientation relationship, such that its orientation follows [46]:

$$\mathbf{T}_{\mathrm{twin}}^{\beta} = \mathbf{Q}^{\beta}\mathbf{T} \tag{3}$$

where $\mathbf{Q}^{\beta} = 2\mathbf{n}_{\mathrm{twin}}^{\beta} \otimes \mathbf{n}_{\mathrm{twin}}^{\beta} - \mathbf{I}, \mathbf{n}_{\mathrm{twin}}^{\beta}$ is the twin plane unit normal of the twin system β, and $\mathbf{I}$ is the identity tensor.

Inspired by Kalidindi [23], the plastic velocity gradient, $\mathbf{L}^{\mathrm{p}}$, has contributions from 12 $\{1\,1\,1\}\langle 1\,1\,0\rangle$ dislocation slip systems, 12 $\{1\,1\,1\}\langle 1\,1\,2\rangle$ twinning systems, and an extra six "virtual" shear band systems:

$$\mathbf{L}^{\mathrm{p}} = \sum_{\alpha=1}^{12} \dot{\gamma}^{\alpha}\mathbf{m}^{\alpha} \otimes \mathbf{n}^{\alpha} + \sum_{\beta=1}^{12} \dot{\gamma}^{\beta}\mathbf{m}_{\mathrm{twin}}^{\beta} \otimes \mathbf{n}_{\mathrm{twin}}^{\beta} + \sum_{\chi=1}^{6} \dot{\gamma}^{\chi}\mathbf{m}_{\mathrm{sb}}^{\chi} \otimes \mathbf{n}_{\mathrm{sb}}^{\chi} \tag{4}$$

The vectors $\mathbf{m}$ and $\mathbf{n}$ denote the directions and plane normals of the deformation systems on which shear occurs at a rate of $\dot{\gamma}$. By omitting the volume fraction of the non-twinned crystal portions in the contribution of dislocation slip in Eq. (4) (in contrast to Ref. [23]), we (i) assume that twins can be sheared by dislocation slip in a compatible manner to the surrounding matrix, and (ii) ignore any potentially different evolution of slip resistance within them.

3.1.2. Dislocation slip and mechanical twinning

The microstructure is parameterized in terms of unipolar and dipolar dislocation densities, ρ_{sgl} and ρ_{dip}, and twin volume fractions f. Following the work of Blum and

Author's personal copy

Eisenlohr [45] the evolution of dislocation densities is related to dislocation multiplication, dipole formation as well as dislocation annihilation. The flow rule describes thermally activated dislocation motion through forest dislocations. The shear rate of the slip system α is:

$$\dot{\gamma}^{\alpha} = \rho^{\alpha}_{\mathrm{sgl}} b v_0 \exp\left[\left(-\frac{Q_0}{k_{\mathrm{B}}T}\left(1-\frac{|\tau^{\alpha}|}{\hat{\tau}^{\alpha}}\right)^{p}\right)^{q}\right]\mathrm{sign}(\tau^{\alpha}) \tag{5}$$

where τ^{α} is the current resolved shear stress; $\hat{\tau}^{\alpha}$ is the slip resistance governed by the dislocation population; b is the length of the Burgers vector; v_0 is the dislocation velocity of the slip system when subjected to a stress equal to the slip resistance $\hat{\tau}^{\alpha}$; Q_0 is the activation energy for dislocation slip; k_{B} and T denote the Boltzmann constant and temperature, respectively; p and q are numerical parameters to adjust the obstacle profile [40]. The slip resistance $\hat{\tau}^{\alpha}$ depends on the local dislocation densities as:

$$\hat{\tau}^{\alpha} = \tau_{\mathrm{solute}} + Gb\left(\sum_{\alpha'=1}^{N\mathrm{slip}} \xi_{\alpha\alpha'}\left(\rho^{\alpha'}_{\mathrm{sgl}} + \rho^{\alpha'}_{\mathrm{dip}}\right)\right)^{1/2} \tag{6}$$

with τ_{solute} a constant resistance from solid solution, G the shear modulus, and $\xi_{\alpha\alpha'}$ characterizes the interaction strength between different slip systems α and α' as a result of the possible interaction types of self, coplanar, collinear, orthogonal, glissile and sessile [47].

The evolution of the volume fractions f^{β} for twin systems is based on the twin nucleation scheme proposed by Mahajan et al. [48]. It is assumed that the critical twin nucleation event is the correlated bow-out of three partial dislocations between pinning points separated by L_0. Then, the critical stress for twin formation is calculated as

$$\hat{\tau}_{\mathrm{twin}} = \frac{\gamma_{\mathrm{sf}}}{3b_{\mathrm{twin}}} + \frac{3Gb_{\mathrm{twin}}}{L_0} \tag{7}$$

where b_{twin} is the Burgers vector of the moving partials and γ_{sf} is the stacking fault energy of the material. Using this critical stress the twin nucleation rate is expressed as

$$\dot{N}^{\beta} = \dot{N}_0 \exp\left[-\left(\frac{\hat{\tau}_{\mathrm{twin}}}{\tau^{\beta}}\right)^{r}\right] \tag{8}$$

where τ^{β} is the resolved stress in the twin system, and $\dot{N}_0$ and r are fitting parameters. We assume that any twin grows instantaneously until it encounters an obstacle, such as a grain or twin boundary. The volume of the new twin is

$$V^{\beta} = \frac{\pi}{6} s \lambda^{\beta 2} \tag{9}$$

Here, s is a constant twin thickness, and λ^{β} is the effective distance between obstacles against twin growth:

$$\frac{1}{\lambda^{\beta}} = \frac{1}{d_{grain}} + \sum_{\beta'=1}^{12} \xi_{\beta\beta'} \frac{1}{d^{\beta'}_{twin}} \tag{10}$$

d_{grain} is the constant grain size, and d_{twin} evolves with twin volume fractions as:

$$d^{\beta}_{\mathrm{twin}} = s(1-f)/f^{\beta} \tag{11}$$

with f the total volume fraction of twins. The twin–twin interaction parameter $\xi_{\beta\beta'}$ is 0 for coplanar twin systems β and β' and 1 for non-coplanar systems. Then, the resulting shear rate for each twin system is calculated as

$$\dot{\gamma}^{\beta} = (1-f)\gamma_{\mathrm{twin}} V^{\beta} \dot{N}^{\beta} \tag{12}$$

where γ_{twin} is the characteristic twin shear. Details of the dislocation and twinning models are described in Refs. [45,40].

3.1.3. Shear banding

The additional incorporation of shear banding into the constitutive model is motivated by the fact that these non-crystallographic defects occur in low SFE alloys when further slip of dislocations is inhibited by the presence of dense twin boundaries as reported in Refs. [1,2,6,8–10]. The use of shear band models in metallic materials was suggested by Anand for amorphous [39] and nanocrystalline materials [49]. In this model deformation occurs on specific non-crystallographic shear banding systems. These are defined relative to the three (variable) principal directions of the second Piola–Kirchoff stress $\mathbf{T}^{\mathrm{e}}$ (conjugated to the elastic Green–Lagrange strain).[1] This is a major difference to other approaches [50,51] that used additional fixed crystallographic systems ($\{1\,1\,1\}\langle 1\,1\,2\rangle$) to model shear banding.

The spectral decomposition of the Piola–Kirchoff stress $\mathbf{T}^{\mathrm{e}}$ reads:

$$\mathbf{T}^{\mathrm{e}} = \sum_{i=1}^{3} \sigma_i \hat{\mathbf{e}}_i \otimes \hat{\mathbf{e}}_i \tag{13}$$

where σ_i are the principal stresses and $\hat{\mathbf{e}}_i$ the orthonormal principal directions of $\mathbf{T}^{\mathrm{e}}$. According to Anand's approach, shear banding in the current model does not proceed on preferred crystallographic directions as dislocation slip or twinning. Therefore, the plastic flow due to shear banding is considered on six potential systems in the planes constructed by the three principal stress directions. In each $(\hat{\mathbf{e}}_i$–$\hat{\mathbf{e}}_j)$-plane, the two potential shear band systems are specified by a direction $\mathbf{m}$, and a plane normal $\mathbf{n}$:

$$\begin{aligned}
\mathbf{m}^{(1)} &= \cos(\pi/4)\hat{\mathbf{e}}_i + \sin(\pi/4)\hat{\mathbf{e}}_j,\\
\mathbf{n}^{(1)} &= \sin(\pi/4)\hat{\mathbf{e}}_i - \cos(\pi/4)\hat{\mathbf{e}}_j\\
\mathbf{m}^{(2)} &= \cos(\pi/4)\hat{\mathbf{e}}_i - \sin(\pi/4)\hat{\mathbf{e}}_j,\\
\mathbf{n}^{(2)} &= \sin(\pi/4)\hat{\mathbf{e}}_i + \cos(\pi/4)\hat{\mathbf{e}}_j
\end{aligned} \tag{14}$$

where the indices i and j range from 1 to 3 with $i \neq j$. The superscripts on $\mathbf{m}$ and $\mathbf{n}$ denote the identifier of each system.

In order to be able to formulate a kinetic equation for shear band formation similar to crystallographic slip

[1] The non-crystallographic shear band systems in Refs. [39,49] are actually defined with respect to the Mandel stress $\mathbf{M}^{\mathrm{e}} = \mathbf{C}^{\mathrm{e}}\mathbf{T}^{\mathrm{e}}$, where $\mathbf{C}^{\mathrm{e}} = \mathbf{F}^{\mathrm{e}^{\mathrm{T}}}\mathbf{F}^{\mathrm{e}}$ ($\mathbf{F}^{\mathrm{e}}$ is the elastic deformation gradient). In single crystals with anisotropic elasticity, $\mathbf{M}^{\mathrm{e}}$ is not symmetric. However, if one makes the approximation $\mathbf{C}^{\mathrm{e}} \approx \mathbf{I}$ ($\mathbf{I}$ is the identity tensor), then the Mandel stress is approximately symmetric and it yields $\mathbf{M}^{\mathrm{e}} \approx \mathbf{T}^{\mathrm{e}}$.

Author's personal copy

(Eq. (5)), we adopt the proposition of Ref. [49] because a strain softening criterion, which is also discussed for low SFE fcc alloys [12,13], is difficult to implement in the current framework. Thus, the governing condition for the "nucleation" of shear bands is shifted from a diminishing strain hardening to the attainment of a critical resolved stress, i.e. a resistance to shear banding. The shear rate $\dot{\gamma}^{\chi}$ for the shear band system χ is formulated in analogy to that for dislocation slip systems:

$$\dot{\gamma}^{\chi} = \dot{\gamma}_0^{\chi} \exp\left[\left(-\frac{Q_0}{k_B T}\left(1 - \frac{|\tau^{\chi}|}{\hat{\tau}_{sb}}\right)^{p}\right)^{q}\right] \mathrm{sign}(\tau^{\chi}) \qquad (15)$$

where $\dot{\gamma}_0^{\chi}$ is a reference shear rate, τ^{χ} is the resolved stress on system χ, and $\hat{\tau}_{sb}$ is the constant threshold stress for shear banding.

3.1.4. FEM implementation

Based on the constitutive laws outlined above, CPFE texture simulations are carried out using the finite element solver MSC.Marc2010 together with a user defined material subroutine. The FE mesh includes 250 eight-noded, isoparametric, three-dimensional brick elements. By assigning four grains (with different orientations) to each of the eight integration points in each element, the total number of initial orientations representing the random texture of the as-received material is $250 \times 8 \times 4 = 8000$. The four grains placed at each integration point are homogenized by a Taylor-type [52] local homogenization. For predicting rolling textures, plane strain compression with a strain rate of $10^{-3}\ s^{-1}$ is simulated to approximate the rolling process and periodic boundary conditions are adopted.

3.2. Material parameters

The constitutive parameters are determined by fitting the macroscopic stress–strain (σ–ε) and the strain-hardening ($d\sigma/d\varepsilon$–σ) curves obtained from uniaxial compression tests of α-brass [53]. Fig. 2 shows the measured stress–strain curve and the strain-hardening response, which is more indicative of specific deformation mechanisms occurring at different stages of deformation. Below ~150 MPa the decrease of the strain-hardening rate indicates that dislocation slip is the main mechanism. At a stress level above ~150 MPa, the increasing strain-hardening is related to mechanical twinning. Above ~300 MPa the strain-hardening rate starts to drop again, indicating the saturation of the twin volume fraction. We first fitted those parameters in the model that are related to dislocation slip (τ_{solute}, Q_{SD}, Q_0, p, and q) using the deformation stage below 150 MPa. To fit the remaining parameters and fine-tune the dislocation slip-related parameters, the stress regime between 150 MPa and 300 MPa is additionally employed. With this two-stage procedure we could well reproduce both experimental curves at the various stages of deformation (Fig. 2). The optimized constitutive parameters are listed in Table 1. The simulated twin volume fraction as a function of strain is presented in Fig. 2c, showing that ~11 vol.% of the material is twinned at a strain of 0.25. This agrees well with El-Danaf's [54] experimental observation on the same material with an average grain size of 30 μm.

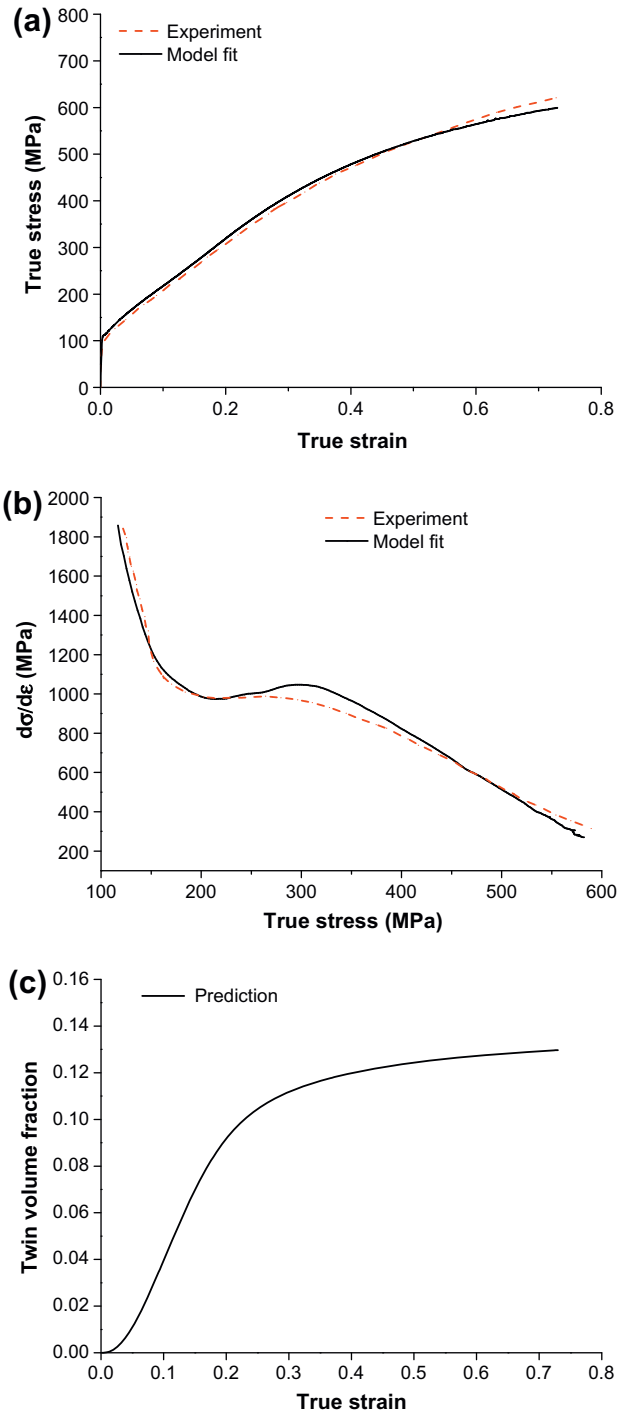

Fig. 2. (a) Stress–strain relation and (b) strain-hardening response of α-brass in uniaxial compression. The experimental data set is obtained from Ref. [53]. (c) Predicted evolution of twin volume fraction with increasing true strain.

Author's personal copy

Table 1
Constitutive material parameters of α-brass used for the crystal plasticity simulations of plane strain compression. C_{11}, C_{12} and C_{44} are the single crystal elastic constants.

C_{11}	C_{12}	C_{44}	d_{grain}	s	b	$\rho_{sgl,0}$
147.0 GPa	111.0 GPa	72.0 GPa	30 μm	0.1 μm	2.56×10^{-10} m	1.0×10^{12} m^{-2}
$\rho_{dip,0}$	v_0	D_0	τ^*_{solute}	Q^*_{SD}	Q^*_0	p^*
1.0 m^{-2}	1.0×10^{-4} m·s^{-1}	3.4×10^{-5} m^2·s^{-1}	0.033 GPa	2.7×10^{-19} J	4.0×10^{-19} J	1.15
q^*	b_{twin}	γ_{sf}	L^*_0	N^*_0	r^*	$\dot{\gamma}^{\chi}_0$
1.0	1.47×10^{-10} m	0.015 J m^{-2}	$520 \times b$	5.0×10^{14} s^{-1}	2.0	1.0×10^{-4} m s^{-1}

Regarding the thermal activated annihilation of dislocations, the following parameters are used: $\rho_{sgl,0}$ and $\rho_{dip,0}$ are the initial dislocation density and dipole density, respectively; v_0 is the initial glide velocity; D_0 is the bulk diffusion coefficient; and Q_{SD} is the activation energy for dislocation climb. The asterisk (∗) indicates fitting parameters.

4. Simulation of rolling textures

Textures of fcc metals can be described in terms of three characteristic fibers, namely, the α, β, and τ fibers [1]. Fig. 3a–c shows the measured and the simulated orientation densities along these fibers. The texture measurements by Hirsch et al. [1] on Cu–30 wt.% Zn are also presented for comparison. The simulated textures are obtained from three models incorporating different specific deformation mechanisms: (i) dislocation slip only, denoted hereafter as "Slip" model; (ii) dislocation slip and mechanical twinning, referred to as "Slip + Twin" model; (iii) dislocation slip, twinning and shear banding, denoted as "Slip + Twin + SB" model. At low strains, i.e. 20% thickness reduction, the Goss, brass, and copper texture components are reproduced by all three model variants. However, after 40% reduction, differences among the three model predictions appear. This can be seen in the β and τ fibers in terms of the copper component (Fig. 3b and c): a significant increase of the copper and S components (copper-type textures) is predicted by the slip and Slip + Twin models. At higher strains, in both simulations an additional increase of the $\{1\,1\,1\}\langle 2\,1\,1\rangle$ component (brass-R) is identified. This agrees with the experimental ODFs, which reveal that some $\{1\,1\,1\}$ fiber components are formed after a deformation of 40%. Moreover, the copper component further develops and very sharp copper-type textures appear at 80% and 90% reductions. A smaller increase of the copper component is predicted by the Slip + Twin model. Nevertheless, both simulations (slip and Slip + Twin) deviate from the experimental results that exhibit a stronger brass component compared to the copper component at large reductions. The discrepancy between the two experimental data sets (our own measurements and the literature data of Hirsch et al. [1]) is ascribed to the different starting microstructures and textures. By showing the spread in the available experimental data, we aim at emphasizing that it is not adequate to compare predictions to one data set only, owing to the scatter inherent to experiments in terms of microstructure, texture, and processing conditions.

The experimental textures at large reductions (above 80%) are apparently not of copper-type as would be expected from homogeneous dislocation shear deformation. We hence suggest that shear bands might be responsible for the texture evolution in low SFE fcc materials. Using the newly developed Slip + Twin + SB model in conjunction with a critical stress to initiate shear banding ($\hat{\tau}_{sb}$) of 0.3 GPa, stronger brass-type textures are predicted compared to the simulations without shear banding, as can be seen from the α fiber at 60% reduction. Also, we observe that both the copper and the brass-R components are less pronounced when compared to the predictions obtained by the slip and the Slip + Twin models. When using an activation stress of $\hat{\tau}_{sb} = 0.18$ GPa for shear banding, the brass component is continuously strengthened with increasing deformation up to a strain of 90%. The Goss component does not show a significant increase as was predicted by the Slip + Twin + SB model when using 0.3 GPa activation stress. Comparison of the two shear band simulations with different threshold stresses reveals that an easier activation of shear banding ($\hat{\tau}_{sb} = 0.18$ GPa) leads to a more pronounced suppression of the development of the copper and S components. Still, there is a discrepancy between the prediction and the measurements. That is, for the α fiber at a reduction of 60%, the predicted texture component with the maximum intensity is located at $\varphi_1 = 34.9°$, which is ∼5° above the one observed in experiments. With continued deformation, this discrepancy increases and reaches 7° deviation at 80% reduction. With increasing strain a shift of the peak position also occurs in the measured orientation distributions on the α fiber [1]. According to the literature data, during rolling from 60% to 80% the peak position on the α fiber is shifted by 3°; with continued deformation, a further increase of 4° is observed from 80% reduction up to 99% [1].

It should be mentioned that the insufficient prediction of the exact orientation density of the brass component via crystal plasticity models is a long-standing problem also for medium and high SFE fcc metals that do not deform via twinning and shear banding [55]. The Slip + Twin + SB model presented here quantitatively captures the evolution of the brass-type textures in α-brass, although the copper component is not weakened as much as observed in experiments. This means that for low SFE metals at large strains, the non-crystallographic shear banding mechanism

Author's personal copy

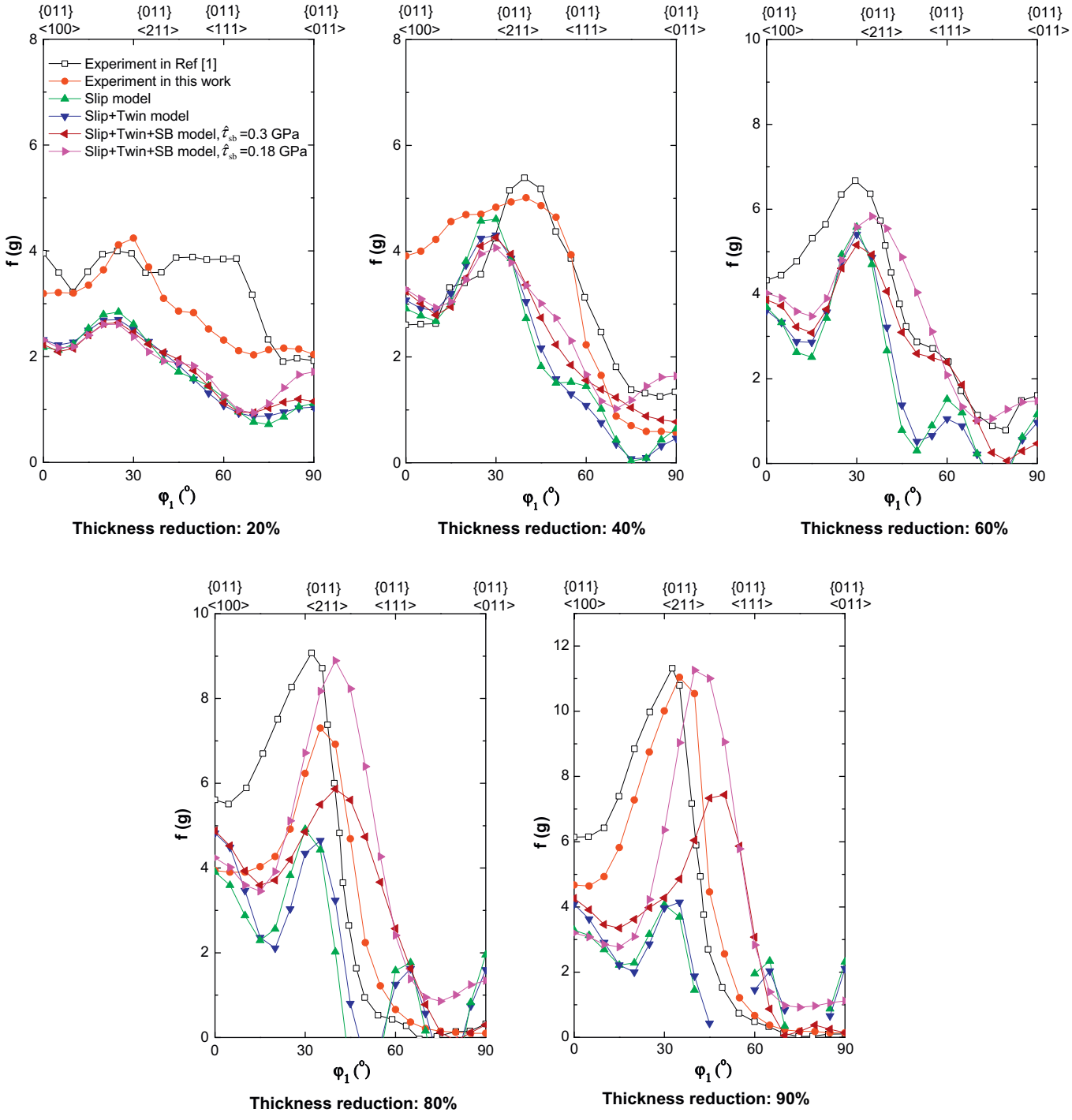

(a) α fiber

Fig. 3. Texture evolution of cold rolled α-brass at different thickness reductions in fiber representation. (a) α fiber with constant Euler angles $\Phi = 45°$ and $\varphi_2 = 0°$, (b) β fiber with local maximum texture intensity along a skeleton line (with variable coordinates), and (c) τ fiber with constant Euler angles $\varphi_1 = 0°$ and $\varphi_2 = 45°$. $\hat{\tau}_{sb}$ is the threshold stress for shear band initiation. The simulated textures are obtained from three models incorporating different deformation mechanisms: (i) dislocation slip only, denoted as slip model; (ii) dislocation slip and mechanical twinning, denoted as slip + twin model; (iii) dislocation slipping, twinning and shear banding, denoted as slip + twin + SB model.

might be the reason for not only suppressing the copper-type texture but also for strengthening the brass-type texture. Hence, by introducing shear banding into constitutive CPFE models, we expect to yield texture predictions for fcc alloys that have a better agreement to experiments and better reflect the real microstructure evolution of heavily strained metals in terms of accounting for non-crystallographic shear contributions.

Author's personal copy

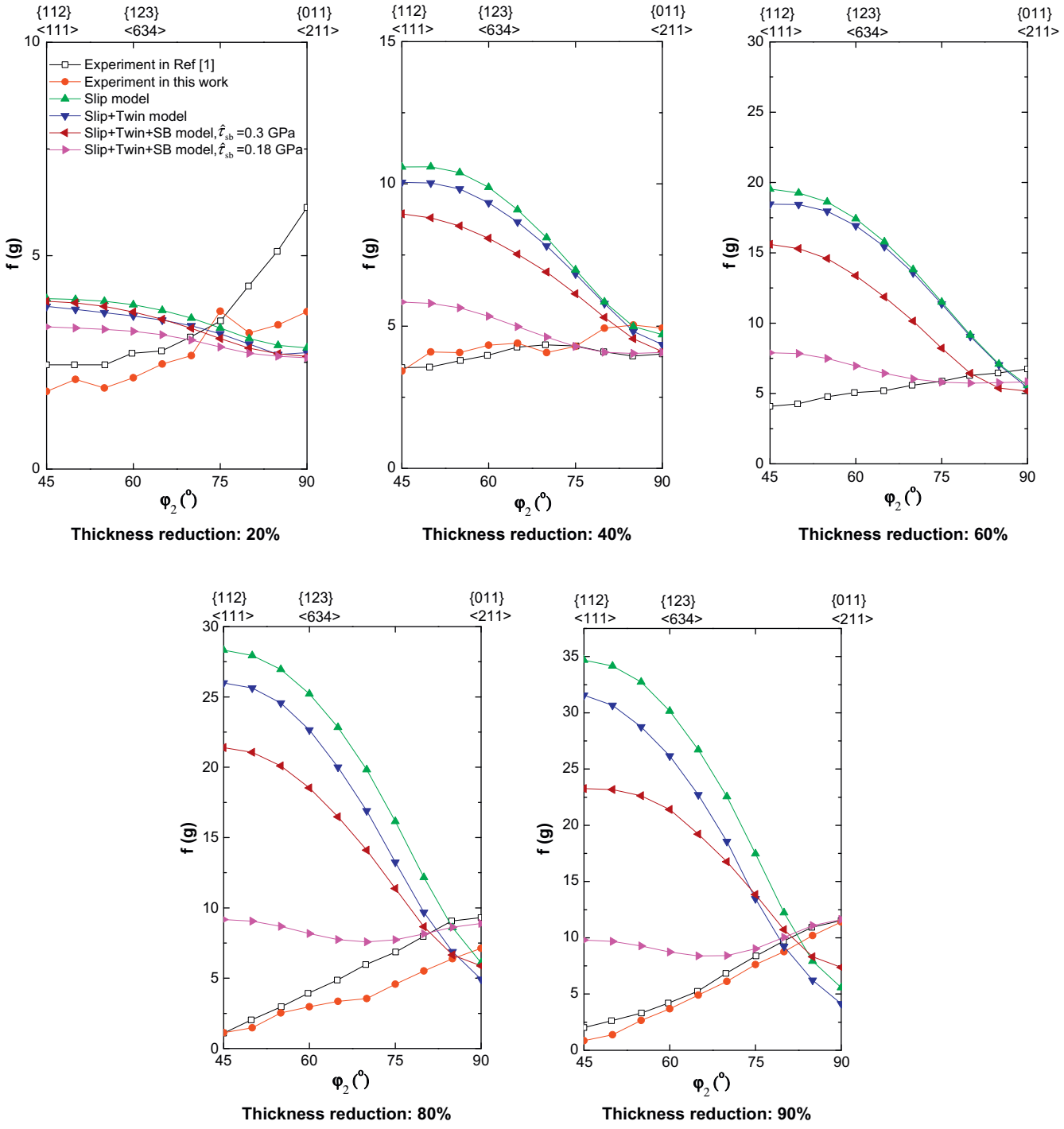

(b) β fiber

Fig 3. *(continued)*

5. Discussion

5.1. Effects of shear banding on texture evolution

The shear rates on the competing deformation systems (dislocation slip, twinning, shear banding) obtained from the different simulations are plotted as a function of the strain in compression direction in Fig. 4. The shear rates are given as summations over the absolute values on the different systems for each type of deformation mechanism. Consequently, in the simulation incorporating dislocation slip only (Fig. 4a), the shear rate on the slip systems remains on a constant level during plastic straining. For the simulation considering dislocations and twins (Fig. 4b), an increase in the twinning shear rate is predicted at the initial stage of deformation, and the maximum

Author's personal copy

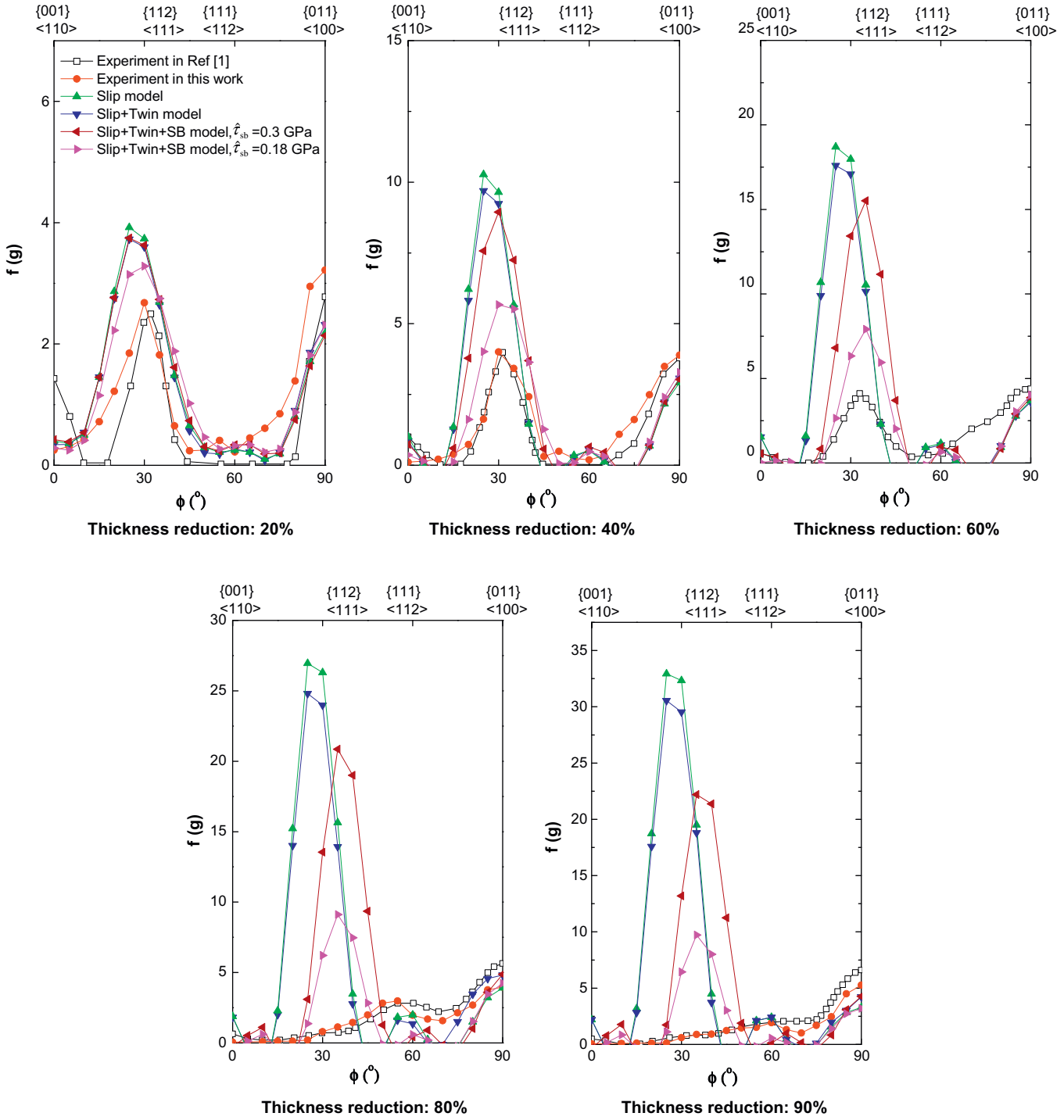

(c) τ fiber

Fig 3. *(continued)*

occurs at a strain of 0.1. With further deformation, the shear rate of the dislocations increases, indicating that the material is deformed both by dislocation slip and by twinning. Besides these differences in the shear rates, the Slip model and the Slip + Twin model predict similar textures. However, a smaller increase of both the copper and brass components is predicted by the Slip + Twin model at a reduction of 40% (strain $\varepsilon = 0.51$). This indicates that mechanical twinning (Fig. 5) provides only a small contribution to the texture transition from copper to brass type.

For the Slip + Twin + SB simulation with 0.30 GPa threshold stress for shear banding (Fig. 4c), at the initial stage of deformation dislocations and twins provide similar shear contributions as in the models without shear

Author's personal copy

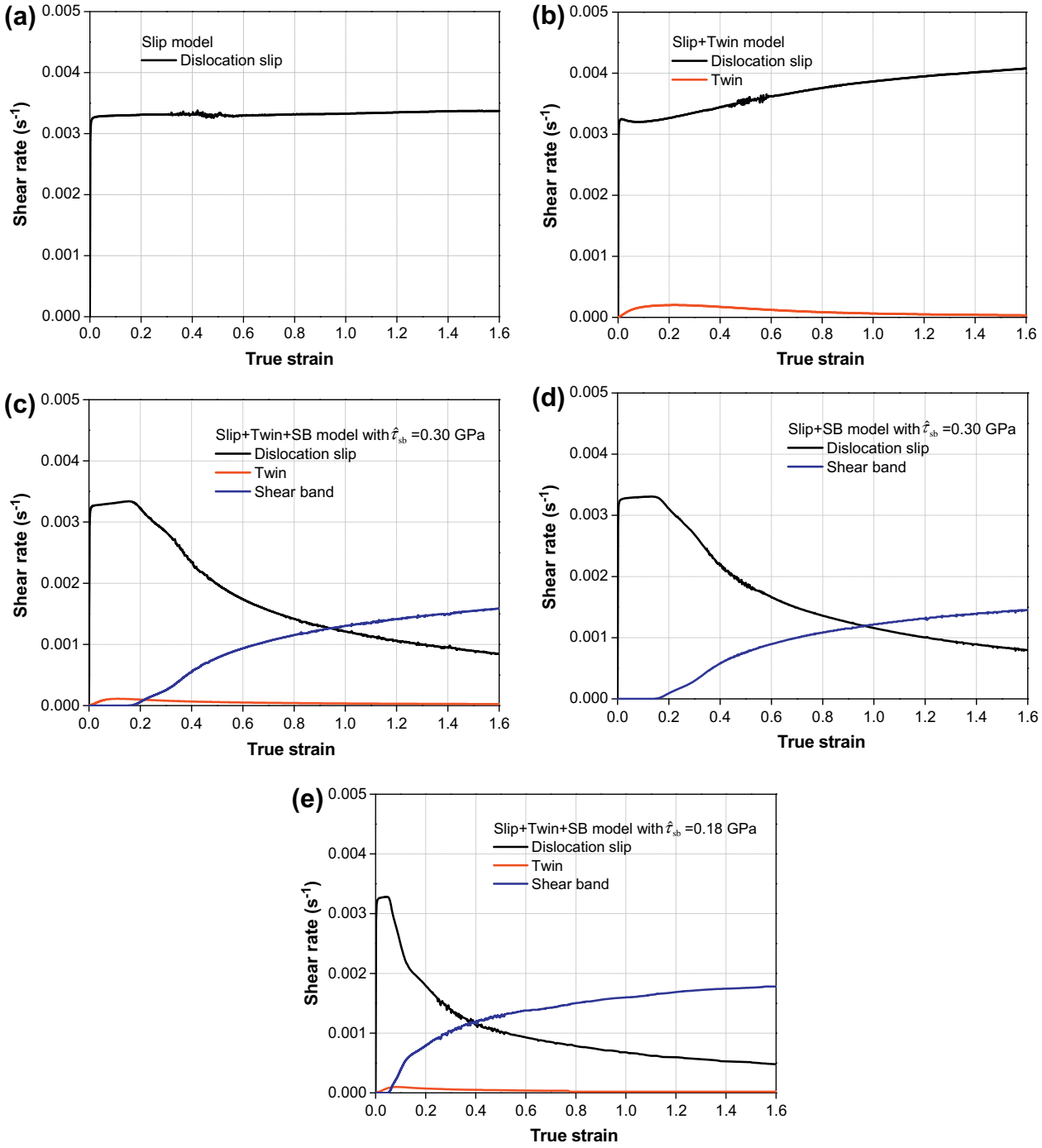

Fig. 4. Predicted average shear rates on the respective deformation systems (dislocation slip, twin and shear band) as a function of true strain along the compression axis by using: (a) slip model, (b) slip + twin model, (c) slip + twin + SB model with the threshold stress for shear banding of 0.30 GPa, (d) slip + SB model, and (e) slip + twin + SB model with the threshold stress for shear banding of 0.18 GPa. $\hat{\tau}_{sb}$ is the threshold stress for shear band initiation.

banding. At a strain of 0.15, the shear rate from dislocation slip drops and the shear rate contributed by shear bands increases. This means that shear banding increasingly carries the deformation. At 0.9 strain, the shear rate on the shear band systems is higher than that provided by both dislocations and twins. The predicted evolution of the shear rates matches experimental observations in cold-rolled α-brass [1,2,12]: These works show that shear banding starts to dominate over the other deformation mechanisms at a reduction of 60% (0.92 strain). The evolution of shear rates obtained by a simulation without twinning (Slip + SB model) is presented in Fig. 4d. Compared to the Slip + Twin + SB simulation, the Slip + SB model shows that after a strain of 0.15 the contribution of shear bands is less pronounced, and that shear banding dominates at a later stage at a strain of 0.95. This result reveals

Author's personal copy

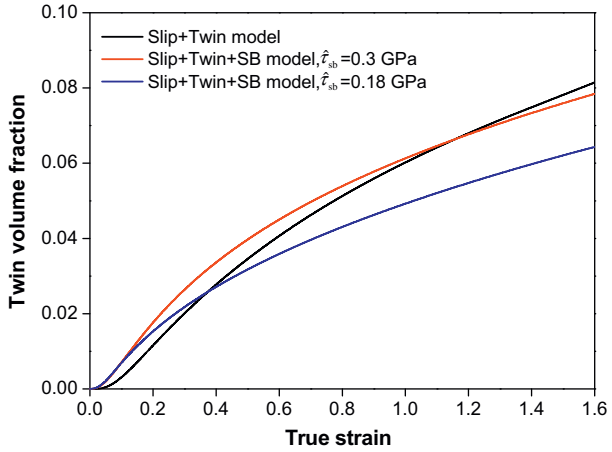

Fig. 5. Predicted twin volume fraction as a function of true strain along the compression axis. $\hat{\tau}_{sb}$ is the threshold stress for shear band initiation.

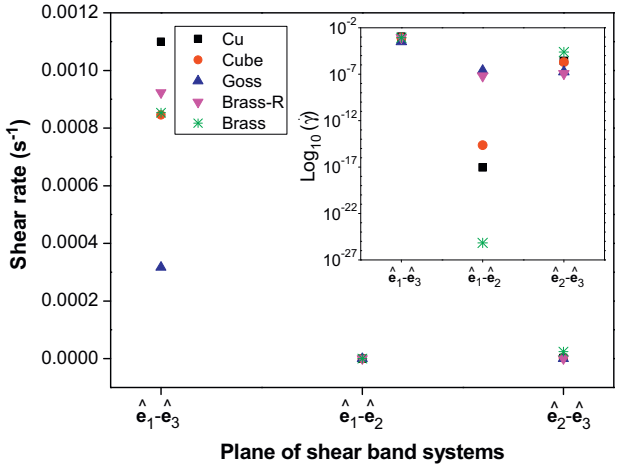

Fig. 6. Predicted shear rates ($\dot{\gamma}$) on particular shear band systems for grains with different initial orientations in α-brass at 60% thickness reduction. $\hat{\mathbf{e}}_i$ are the orthonormal principal directions corresponding to the principal stresses σ_i.

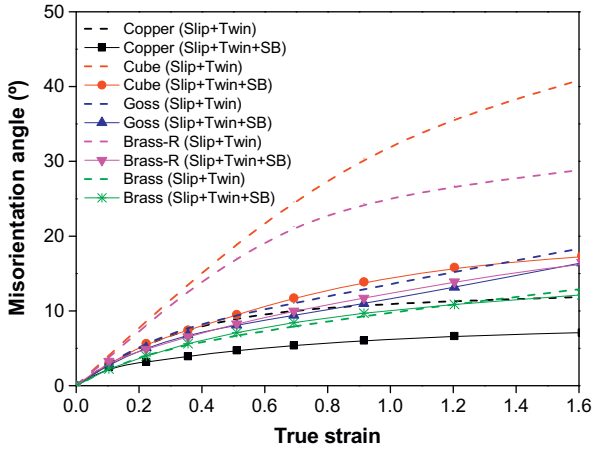

Fig. 7. Predicted misorientation angles for grains with different initial orientations as a function of true strain. The misorientation angle is defined relative to the initial orientation of each group of grains.

that the development of shear bands is facilitated by shear strain accumulation in twinned structures [8,11,13]. The texture predictions of the Slip + Twin + SB model reveal that shear banding contributes to the suppression of copper-type textures as well as to the promotion of brass-type textures. Consequently, we expect a dependence of this phenomenon on the critical stress for shear band activation. For a threshold stress of 0.18 GPa, a sharp decrease in the shear rate contribution from dislocations is predicted at an early stage of deformation (below 0.1 strain), as shown in Fig. 4e. According to this simulation, the shear rates on dislocation slip systems and twin systems are lower than predicted by the other model variants. This is attributed to the fact that deformation proceeds mainly via shear banding rather than via dislocation slip and twinning. It is also worth noting that at a strain of 0.4, when shear banding starts to dominate, the copper-type textures are much weaker than in the other simulations. However, the contribution of shear banding to the development of brass-type textures is only observed after a thickness reduction of 60% (0.92 strain), as shown by the β fibers in Fig. 3b. For instance, at 60% reduction, the Slip + Twin model predicts orientation densities of 17 and 4.7 for the copper and brass components, respectively. The Slip + Twin + SB model ($\hat{\tau}_{sb} = 0.18$ GPa) predicts an intensity of 7.9 for the copper component. For the brass component, a minor contribution of shear banding is substantiated from the slightly increased intensity of 5.8. At higher strain levels, the suppression of the copper component and the strengthening of the brass component become more evident. At 80% reduction ($\varepsilon = 1.61$), the Slip + Twin + SB model predicts orientation densities of 9.2 and 8.9 for the copper and brass components, respectively. According to the Slip + Twin simulation, intensities of 26 for the copper and 4.9 for the brass components are predicted, respectively.

5.2. Shear band system analysis

Using the simulation with the threshold stress for shear banding of 0.18 GPa as an example, the different shear band systems are examined. The principal stresses that matter for the constitutive shear band law are derived by principal axis transformation from the second Piola–Kirchoff stress tensor. We order these principal stresses according to $|\sigma_1| \geqslant |\sigma_2| \geqslant |\sigma_3|$ with $\sigma_1 \leqslant 0$, $\sigma_2 \leqslant 0$, $\sigma_3 \geqslant 0$ (cf. Eq. (13)). The shear stress in the plane constructed by the two orthonormal principal directions $\hat{\mathbf{e}}_1$ and $\hat{\mathbf{e}}_3$ (corresponding to the maximum compression stress and the tensile stress) mainly promotes shear banding. To show this more clearly, the shear rates of grain groups with different initial orientations within 10° of their respective ideal orientations (copper, cube, Goss, brass-R, and brass) in the 60% deformed material are examined in Fig. 6. At and above that strain level, the effect of shear banding on texture evolution becomes significant. The examined orientation components are frequently observed in fcc metals. We hence extracted

Author's personal copy

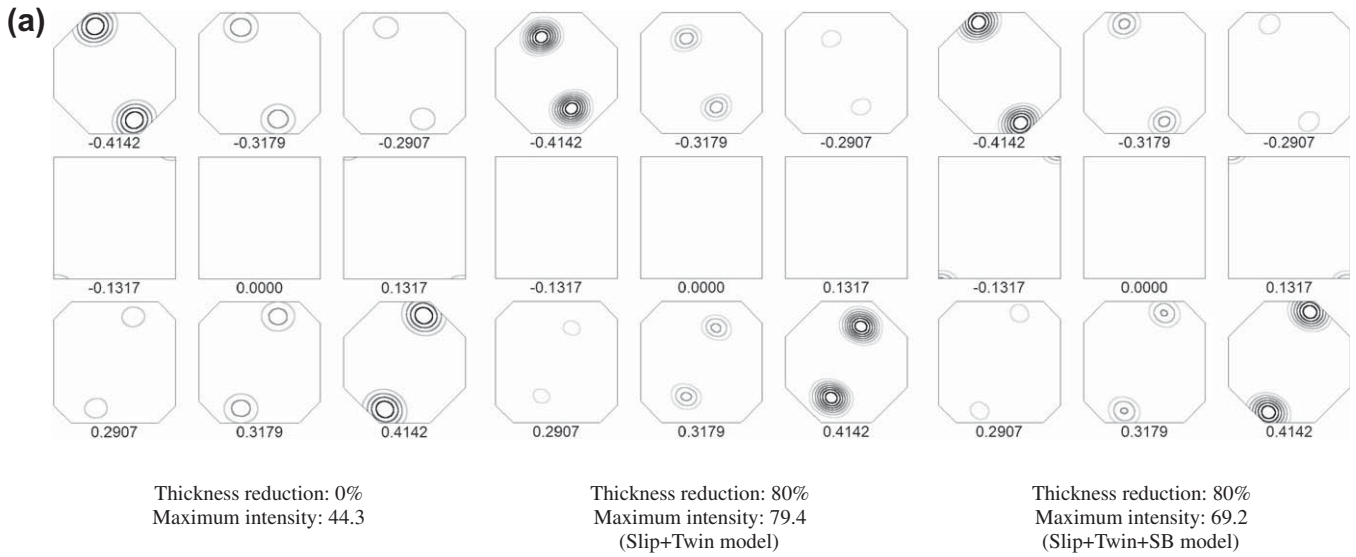

Fig. 8. Predicted ODF on $\mathbf{r}_3$ sections in Rodrigues space of the cubic fundamental region for grains with different initial orientations during plane strain compression: (a) copper, (b) cube, (c) Goss, (d) brass-R and (e) brass. (f) Predicted ODF of α-brass with initial texture of the random type. (g) Positions of ideal texture components represented in Rodrigues space. □ : $\{112\}\langle 111\rangle$ (copper), ■: $\{001\}\langle 100\rangle$ (cube), △: $\{011\}\langle 100\rangle$ (Goss), ▲: $\{111\}\langle 211\rangle$ (brass-R), ▽:$\{011\}\langle 211\rangle$ (brass), ▼: $\{123\}\langle 634\rangle$ (S). The number at the bottom of each section denotes the coordinate of $\mathbf{r}_3$.

the specific shear rates in these orientations from the initial 8000 orientations. For all those five texture components, represented by clusters of similarly oriented grains, the deformation in the $(\hat{\mathbf{e}}_1$–$\hat{\mathbf{e}}_3)$-shear band plane is more significant compared to those in the other planes. In addition, the initially Goss orientated grains exhibit relatively low shear rates, indicating that this texture component is advantageous for preventing shear band development. This result is consistent with an investigation on the effects of different texture components on the formability of aluminum alloys [56].

Besides these orientation-dependent effects of shear banding, it is of interest to note that shear bands contribute to high shear rates under plane strain constraints, but due to the symmetric distribution of the shear about the principal stress directions they may contribute only little to the rotation rates. Fig. 7 shows the evolution of the misorientation angles for initially differently orientated grains during deformation as obtained from the Slip + Twin and Slip + Twin + SB models. The Slip + Twin simulation shows that rotation rates of the cube and the brass-R orientated grains are much higher than those of the other grains. Comparison of the two simulations reveals that shear banding leads to smaller rotation rates for all grain groups except for the brass component. With continued strain, the difference among the simulations increases,

Author's personal copy

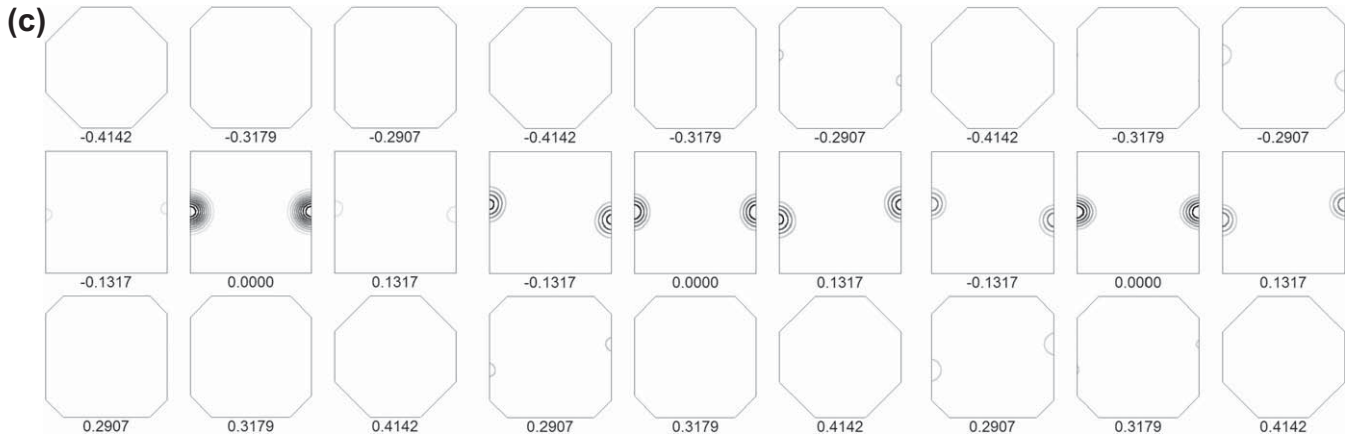

Thickness reduction: 0%
Maximum intensity: 97.1

Thickness reduction: 80%
Maximum intensity: 43.5
(Slip+Twin model)

Thickness reduction: 80%
Maximum intensity: 60.4
(Slip+Twin+SB model)

Initial orientation of grains: Goss (Contour levels: 10.0, 20.0…)

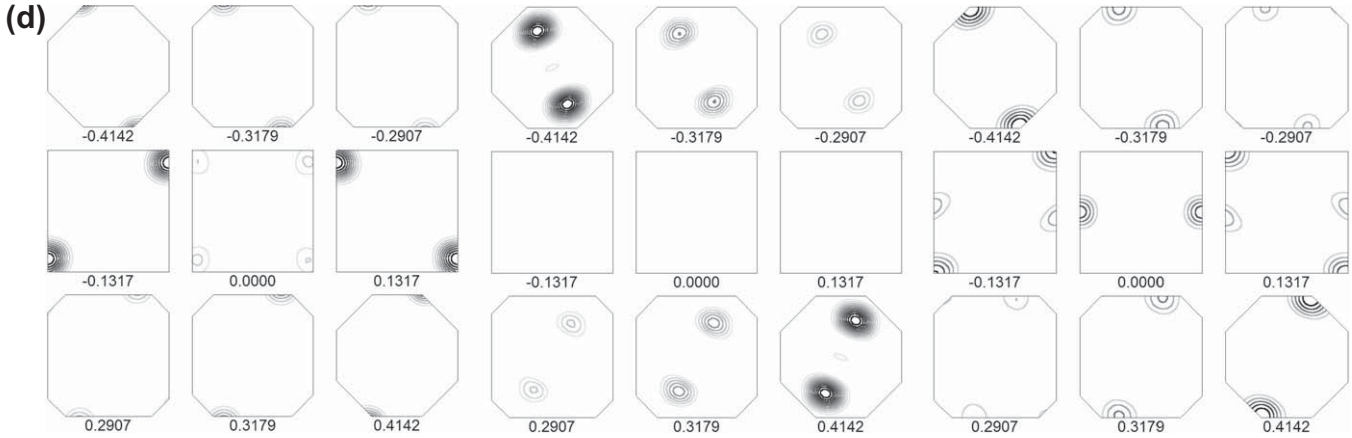

Thickness reduction: 0%
Maximum intensity: 46.4

Thickness reduction: 80%
Maximum intensity: 56.4
(Slip+Twin model)

Thickness reduction: 80%
Maximum intensity: 25.2
(Slip+Twin+SB model)

Initial orientation of grains: Brass-R (Contour levels: 5.0, 10.0…)

Fig 8. *(continued)*

suggesting that the shear bands decrease the rotation rates of most orientations.

For better visualizing details of the texture evolution under the effect of shear bands, the calculated ODFs of the grains with different initial orientations at the thickness reduction of 80% are represented in Rodrigues space (Fig. 8a–e). This representation allows one to track texture trends more effectively owing to symmetry effects. The fundamental region of the cubic symmetry group is a truncated cube. For the current analysis ODF sections perpendicular to the $\mathbf{r}_3$ axis of the fundamental region are adequate. Under plane strain compression, the axes $\mathbf{r}_1$, $\mathbf{r}_2$ and $\mathbf{r}_3$ of Rodrigues space correspond to the sample axes RD, TD, and ND, respectively. Some ideal texture components in Rodrigues space are illustrated in Fig. 8g.

The shear band model predicts significant non-crystallographic deformations at moderate reductions for all grain groups. Most orientations seem to be more stable against reorientation compared to the case when shear banding is not initiated. Comparing the predictions of the Slip + Twin and Slip + Twin + SB models, the evolution of the different orientations is discussed in the following. In the model without shear banding, both the copper and S components are significantly strengthened for grains with original copper, cube, and brass-R orientation. For Goss and brass orientated grains, this texture transition is not found. The shear band model reveals that copper grains deviate from their original orientation, accompanied by a minor development of the brass-R component. For the original cube component the texture evolution towards the copper component is impeded. In addition, the transition from the cube component towards the Goss component is evident. For the brass-R grains, a texture transition towards the Goss component is observed. For convenience one should

Author's personal copy

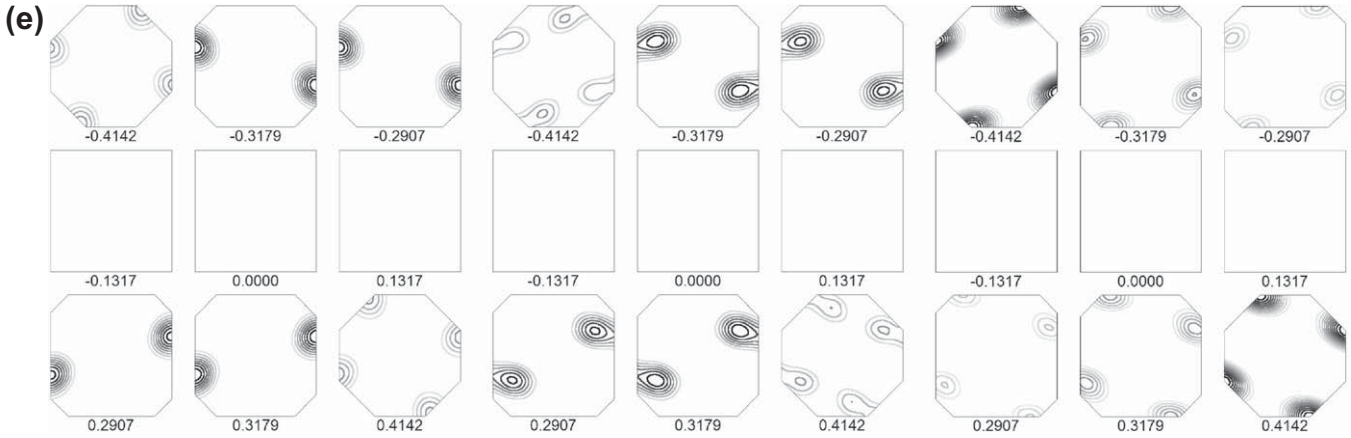

Thickness reduction: 0%
Maximum intensity: 44.1

Thickness reduction: 80%
Maximum intensity: 31.3
(Slip+Twin model)

Thickness reduction: 80%
Maximum intensity: 58.0
(Slip+Twin+SB model)

Initial orientation of grains: Brass (Contour levels: 5.0, 10.0…)

Fig 8. *(continued)*

note that plane strain compression textures appear along the ND $\|$ $\langle 1\,1\,0\rangle$ fibers. For example, the α fiber can be observed on the $\mathbf{r}_1$ face ($\mathbf{r}_1 = \pm 0.4142$). For Goss grains with relatively low shear banding, rotation rates are less influenced. For the brass component, the evolution to the S component is impeded. Moreover, with the use of the shear band model the grain rotation about the $\mathbf{r}_3$ axis is observed. At 80% deformation the initial orientation on the ODF sections at $\mathbf{r}_3 = \pm 0.3179$ moves to the sections at $\mathbf{r}_3 = \pm 0.4142$. This observation corresponds to the predicted α fiber textures in fiber representation showing a shift of the peak position to higher φ_1 angles. The rotation of the brass grains is contributed by the relaxed shear in the ($\hat{\mathbf{e}}_2$–$\hat{\mathbf{e}}_3$)-plane (Fig. 6).

For low SFE metals the lattice rotations inside shear bands have been investigated in Refs. [6,8–11]. However, the contribution of shear bands to the overall textures remained unclear up to now. The current simulations show that with the incorporation of non-crystallographic shear banding into the constitutive model in addition to dislocation and twinning shear, the brass-R, cube and Goss components tend to evolve from their initial orientations towards the brass-type texture. This is in general agreement with the experimental observations in Refs. [8,9,11]. Compared to the Slip + Twin model, the Slip + Twin + SB model predicts a more stable copper component for the grains initially orientated with this orientation. However, significant suppression of texture evolution towards the copper component is also predicted for the other grains according to the shear band simulation. This leads to an overall texture development that can indeed explain the transition from the copper type to the brass type. The predicted ODFs of α-brass with an initially random texture are shown in Fig. 8f. Using the shear band model, at low and moderate reductions ($\leqslant$40%) a homogeneous development of the β fiber connecting the copper, S, and brass components is predicted. With continued strain, the ODF intensities along the α fiber that connects the Goss and brass components on boundaries of the fundamental region (on the $\mathbf{r}_1$ face) also develop. At 80% reduction a stronger development of brass orientation relative to Goss becomes visible.

5.3. Stress–strain response in the context of shear banding

The equivalent true stress–equivalent true strain curves of α-brass obtained from the different simulations are shown in Fig. 9. The Slip + Twin model captures the measurement best. The Slip model shows that the material becomes softer when twinning is not involved. When introducing the non-crystallographic shear banding mechanism, an apparent softening effect on the stress–strain curve is predicted by the Slip + SB and Slip + Twin + SB models. This effect is consistent with shear band theory: As knowledge on how shear banding quantitatively adjusts macroscopic mechanical properties of fcc materials is lacking, in the current work only the constitutive parameters describing dislocation slip and twinning were fitted to give the optimum agreement with the mechanical test. In addition, shear bands are assumed to be softer than their original matrix (twin/matrix lamellar structure) [57]. Concerning the hardening induced by interactions among the shear band systems as proposed in this work, however, no clear physical picture exists yet in the literature. Therefore, in the present model the threshold stress to initiate shear banding is assumed constant, i.e. no additional strain-hardening is introduced that would be specific for shear banding. On the other hand, when shear banding contributes to the overall hardening, the prediction of the mechanical behavior of fcc metals could be improved. This may be achieved by introducing hardening effects associated

Author's personal copy

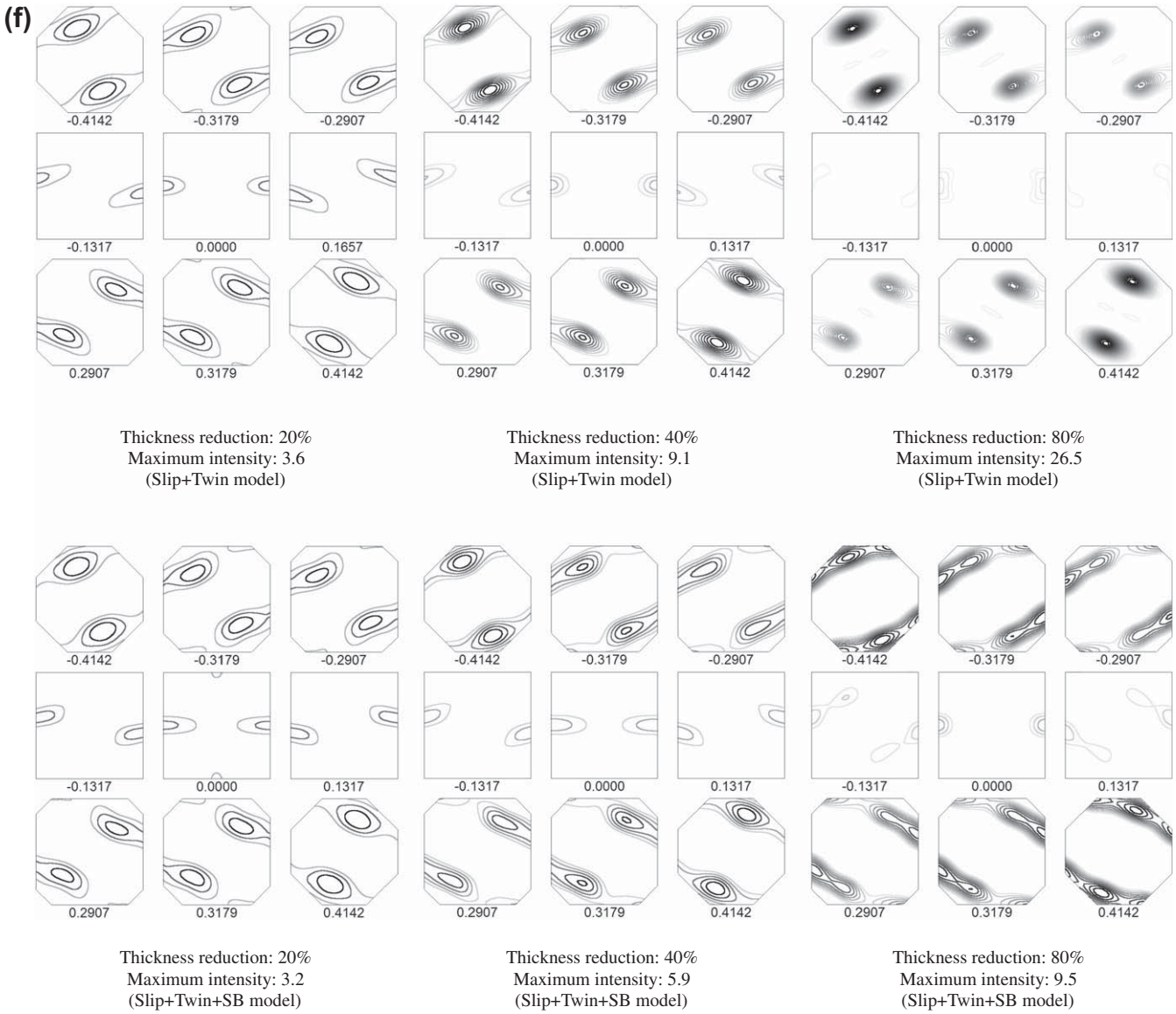

Initial orientation of α-brass: random (Contour levels: 1.0, 2.0…)

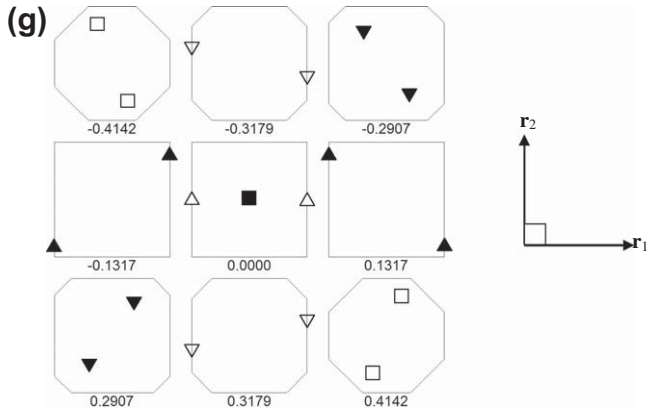

Fig 8. *(continued)*

with shear bands or using tuned constitutive parameters, while a good prediction of the deformation textures is maintained.

In fact, the texture development in α-brass under plane strain deformation is a very clear example for the effect of shear bands and the corresponding microstructures on

Author's personal copy

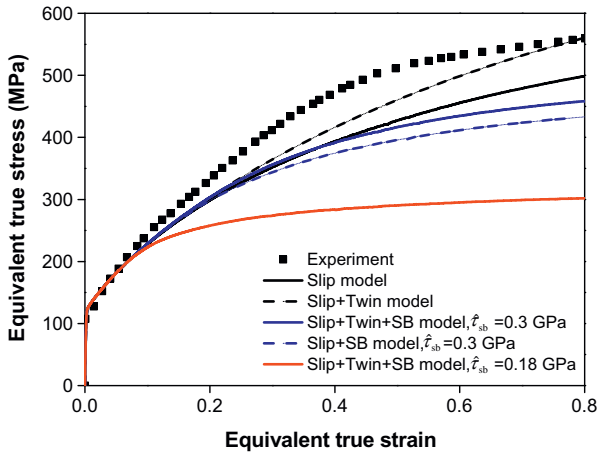

Fig. 9. Predicted equivalent true stress-equivalent true strain responses of α-brass during plane strain compression. The experimental data is obtained from Ref. [53].

texture evolution. In this work, deformation textures of α-brass are predicted by performing a series of simulations with different constitutive models. One of the important findings is that the incorporation of non-crystallographic shear banding scheme in the CPFE model contributes to the texture transition from the copper type to the brass type. However, the deficiency in terms of quantitative predictions of the suppression of the copper-type textures still exists. For even more accurately predicting deformation textures of fcc materials with low SFE, an in-depth investigation that includes the dedicated micromechanisms as well as quantitative influences of grain-to-grain interactions on the lattice rotation is still required. This is, however, beyond the scope of the current paper.

6. Concluding remarks

A shear band model has been developed to simulate deformation textures of low SFE fcc materials. The novelty of the model is that a non-crystallographic shear band mechanism is incorporated in addition to dislocation and twinning shear. By performing finite element simulations incorporating different deformation mechanisms, quantitative comparisons of simulated and experimental textures are evaluated. The main results are as follows:

- Using the models without shear banding (Slip model and Slip + Twin model), the Goss, brass, and copper texture components are predicted at small reductions. At 40% deformation a significant increase in the copper and S components is predicted, and very sharp copper-type textures are obtained even at higher reductions. The elevation of twin volume fraction gives a minor contribution to the texture transition from the copper type to the brass type.
- Activation of shear banding leads to weaker copper and S texture components with increasing deformation, while the intensity of the brass component is increased. The shear band model captures the major aspects of the experimental textures at different stages of deformation.
- Compared to the simulations without shear banding, the model considering shear bands (in addition to dislocations and twins) predicts smaller lattice rotations for grains of different initial orientation. This contributes to the suppression particularly of the copper-type textures. Instead, more grains rotate towards brass-type components. These factors explain the texture transition from the copper type to the brass type.
- A discrepancy in the stress–strain behavior is found between the shear band simulations and experiments, primarily due to the lack of a hardening effect associated with shear banding in the current model.

Acknowledgements

We gratefully acknowledge the financial support of the National Natural Science Foundation of China (Grant Nos. 50725102 and 51101030), the Fundamental Research Funds for the Central Universities (Grant Nos. N090302001 and N090202001), and the Foundation for the Youth Teachers from the Ministry of Education of China (Grant No. 20090042120007). The authors are also grateful to the kind support of the Alexander von Humboldt Stiftung (AvH, Alexander von Humboldt Foundation, www.humboldtfoundation.de) for N. Jia.

References

[1] Hirsch J, Lücke K, Hatherly M. Acta Metall 1988;36:2863.
[2] Duggan BJ, Hatherly M, Hutchinson WB, Wakefield PT. Metal Sci 1978;12:343.
[3] Wassermann G. Z Metallkd 1963;54:61.
[4] Leffers T, Ray RK. Prog Mater Sci 2009;54:351.
[5] Leffers T, Bilde-Sørensen JB. Acta Metall Mater 1990;38:1917.
[6] Donadille C, Valle R, Dervin P, Penelle R. Acta Metall 1989;32:1547.
[7] Raabe D. Acta Mater 1997;45:1137.
[8] Paul H, Driver JH, Maurice C, Piątkowski A. Acta Mater 2007;55:575.
[9] Paul H, Driver JH, Maurice C, Jasieński Z. Mater Sci Eng A 2003;359:178.
[10] Paul H, Driver JH, Jasieński Z. Acta Mater 2002;50:815.
[11] Paul H, Morawiec A, Bouzy E, Fundenberger JJ, Piatkowski A. Metall Mater Trans A 2004;35:3775.
[12] Xiao GH, Tao NR, Lu K. Mater Sci Eng A 2009;513–514:13.
[13] Hong CS, Tao NR, Huang X, Lu K. Acta Mater 2010;58:3103.
[14] Kalidindi SR, Bronkhorst CA, Anand L. J Mech Phys Solids 1992;40:537.
[15] Bronkhorst CA, Kalidindi SR, Anand L. Philos Trans Roy Soc London A 1992;341:443.
[16] Beaudoin AJ, Dawson PR, Mathur KK, Kocks UF, Korzekwa DA. Comput Methods Appl Mech Engrg 1994;117:49.
[17] Becker R, Panchanadeeswaran S. Acta Metall Mater 1995;43:2701.
[18] Clausen B, Lorentzen T, Leffers T. Acta Mater 1998;46:3087.
[19] Dawson PR, Marin EB. Adv Appl Mech 1998;34:77.
[20] Kalidindi SR. J Mech Phys Solids 1998;46:267.
[21] Staroselsky A, Anand L. J Mech Phys Solids 1998;46:671.
[22] Myagchilov S, Dawson PR. Modell Simul Mater Sci Eng 1999;7:975.
[23] Kalidindi SR. Int J Plast 2001;17:837.
[24] Raabe D, Sachtleber M, Zhao Z, Roters F, Zaefferer S. Acta Mater 2001;49:3433.
[25] Raabe D, Zhao Z, Mao W. Acta Mater 2002;50:4379.

Author's personal copy

[26] Raabe D, Roters F. Int J Plast 2004;20:339.
[27] Baczmański A, Braham C. Acta Mater 2004;52:1133.
[28] Roters F, Eisenlohr P, Hantcherli L, Tjahjanto DD, Bieler TR, Raabe D. Acta Mater 2010;58:1152.
[29] Zhao Z, Radovitzky R, Cuitiño A. Acta Mater 2004;52:5791.
[30] Goerdeler M, Gottstein G. Mater Sci Eng A 2001;309–310:377.
[31] Van Houtte P, Delannay L, Kalidindi SR. Int J Plast 2002;18:359.
[32] Schäfer C, Song J, Gottstein G. Acta Mater 2009;57:1026.
[33] Wang H, Raeisinia B, Wu PD, Agnew SR, Tomé CN. 2010;47:2905.
[34] Lebensohn RA, Tomé CN, Maudlin PJ. Int J Plast 2004;52:249.
[35] Lebensohn RA, Brenner R, Castelnau O, Rollett AD. Acta Mater 2008;56:3914.
[36] Liu B, Raabe D, Roters F, Eisenlohr P, Lebensohn RA. Modelling Simul Mater Sci Eng 2010;18:085005.
[37] Engler O, Löchte L, Karhausen K. Mater Sci Forum 2005;495–497:555.
[38] Gil Sevillano J, Van Houtte P, Aernoudt E. Scripta Metall 1977;11:581.
[39] Anand L, Su C. J Mech Phys Solids 2005;53:1362.
[40] Roters F. Habilitation Thesis, RWTH Aachen University, Germany, 2011.
[41] Suiker ASJ, Turteltaub S. Int J Numer Methods Eng 2005;63:1655.
[42] Pawlik K, Ozga P. LaboTex: The Texture Analysis Software, Göttinger Arbeiten zur Geologie und Paläontologie, SB4;1999.
[43] Kocks UF, Tomé CN, Wenk HR. Texture and Anisotropy. Cambridge: Cambridge University Press; 1998.
[44] Kumar A, Dawson PR. Acta Mater 2000;48:2719.
[45] Blum W, Eisenlohr P. Mater Sci Eng A, 2009;510-511:7.
[46] Van Houtte P. Acta Metall 1978;26:591.
[47] Kubin L, Devincre B, Hoc T. Acta Mater 2008;56:6040.
[48] Mahajan S, Chin GY. Acta Metall 1973;21:1353.
[49] Wei YJ, Su C, Anand L. Acta Mater 2006;54:3177.
[50] Wierzbanowski K, in: Gottstein G, Lück K (eds.) Proceedings of the Fifth International Conference on Textures of Materials. Vol. 1. New York: Springer Verlag; 1978, p. 309.
[51] Jia N, Peng RL, Wang YD, Johansson S, Liaw PK. Acta Mater 2008;56:782.
[52] Evers LP, Brekelmans WAM, Geers MGD. J Mech Phys Solids 2004;52:2379.
[53] El-Danaf E, Kalidindi SR, Doherty RD. Int J Plast 2001;17:1245.
[54] El-Danaf E, Kalidindi SR, Doherty RD. Metall Mater Trans A 1999;30:1223.
[55] Li SY, Kalidindi SR, Van Houtte P. Modeling Simul Mater Sci Eng 2004;12:845.
[56] Kuroda M, Tvergaard V. Int J Plast 2007;23:244.
[57] Mishra A, Kad BK, Gregori F, Meyers MA. Acta Mater 2007;55:13.